In Situ Metallic Coating of Atom Probe Specimen for Enhanced Yield, Performance, and Increased Field-of-View

Tim M Schwarz, Eric Woods, Mahander P Singh, Xinren Chen, Chanwon Jung, Leonardo S Aota, Kyuseon Jang, Mathias Krämer, Se-Ho Kim, Ingrid McCarroll, Baptiste Gault

Microscopy and Microanalysis, 2024, **00**, 1–15
https://doi.org/10.1093/mam/ozae006

Original Article

Microscopy AND Microanalysis

In Situ Metallic Coating of Atom Probe Specimen for Enhanced Yield, Performance, and Increased Field-of-View

Tim M. Schwarz[1,*], Eric Woods[1], Mahander P. Singh[1], Xinren Chen[1], Chanwon Jung[1], Leonardo S. Aota[1], Kyuseon Jang[1,2], Mathias Krämer[1], Se-Ho Kim[1,†], Ingrid McCarroll[1], and Baptiste Gault[1,3]

[1]*Department of Microstructure Physics and Alloy Design, Max-Planck-Institut für Eisenforschung, Max-Planck-Str. 1, Düsseldorf 40237, Germany*
[2]*Department of Materials Science and Engineering, Korea Advanced Institute of Science and Technology, 291 Daehak-ro, Yuseong-gu, Daejeon 34141, Republic of Korea*
[3]*Department of Materials, Imperial College London, London SW7 2AZ, UK*

***Corresponding author:** Tim M. Schwarz, E-mail: tim.schwarz@mpie.de

[†]Current address: Department of Materials Science and Engineering, Korea University, Seoul 02841, Republic of Korea.

Abstract

Atom probe tomography requires needle-shaped specimens with a diameter typically below 100 nm, making them both very fragile and reactive, and defects (notches at grain boundaries or precipitates) are known to affect the yield and data quality. The use of a conformal coating directly on the sharpened specimen has been proposed to increase yield and reduce background. However, to date, these coatings have been applied *ex situ* and mostly are not uniform. Here, we report on the controlled focused-ion beam *in situ* deposition of a thin metal film on specimens immediately after specimen preparation. Different metallic targets e.g. Cr were attached to a micromanipulator via a conventional lift-out method and sputtered using Ga or Xe ions. We showcase the many advantages of coating specimens from metallic to nonmetallic materials. We have identified an increase in data quality and yield, an improvement of the mass resolution, as well as an increase in the effective field-of-view. This wider field-of-view enables visualization of the entire original specimen, allowing to detect the complete surface oxide layer around the specimen. The ease of implementation of the approach makes it very attractive for generalizing its use across a very wide range of atom probe analyses.

Key words: atom probe tomography, coating, field of view, mass resolution, yield

Introduction

Atom probe tomography (APT) is a microscopy and microanalysis technique that provides three-dimensional compositional mapping (Larson et al., 2013*a*, 2013*b*, 2013*c*; Lefebvre-Ulrikson et al., 2016; Gault et al., 2021). APT is based on the field evaporation of surface atoms (Forbes, 1995). A field in the range of 10–100 V/nm is generated by applying a high voltage on the order of a few kilovolts to a needle-shaped specimen, with an end radius in the range of 20–100 nm. Superimposed on this electrostatic field are either high-voltage pulses (Müller et al., 1968) or laser pulses (Kellogg & Tsong, 1980; Bunton et al., 2007) that enable time-control of the field evaporation and hence time-of-flight measurement for each ion. Conversely to most other microscopy techniques, the specimen also acts as the primary ion projection optics (Fortes, 1971; Cerezo et al., 1999; De Geuser & Gault, 2017), and control over its shape is hence critical to achieve optimal operation of the atom probe. Specimens can be prepared by electrochemical polishing (Miller & Smith, 1989; Melmed, 1991) or, as increasingly common, by lifting out a piece of the sample, depositing it onto a support and milling it into an appropriate shape using a dual beam scanning-electron microscope–focused-ion beam (SEM-FIB) (Prosa & Larson, 2017).

Needle-shaped substrates have been used as a support to deposit single or multiple layers of a range of materials and enable direct APT analysis. This approach to coat needles has been particularly useful to study materials that were otherwise difficult to prepare into sharp needles, including carbon-based materials for instance (Southon et al., 1975; Prosa et al., 2010; Eder et al., 2017; Zhang et al., 2021), a range of metallic multilayers to study diffusional and interfacial processes (Tamion et al., 2006; Vovk et al., 2007; Larson et al., 2009; Balogh et al., 2011), along with glasses (Greiwe et al., 2014) and thin organic layers (Nishikawa & Kato, 1986; Kelly et al., 2009) or even frozen liquids (Inghram & Gomer, 1955; Stintz & Panitz, 1991; Anway, 2003). The deposition of thin metallic layers on silicon (Schmidt et al., 1988; Jeske et al., 1999), ceramics (Seol et al., 2016), or glass (Kellogg, 1982) was shown to modify the field evaporation behavior, and for laser-pulsed atom probe tomography, it changes the light absorption and heat conduction properties of the specimen. These parameters are critical, since they control the rise and decay time of the "thermal pulse" that triggers field evaporation following laser pulse illumination (Vurpillot et al., 2006, 2009; Houard et al., 2010, 2011), and hence the achievable performance limits of atom probe microanalysis.

Coating of APT specimens has been reported following transfer from the SEM-FIB, through ambient atmosphere, to an external chamber by sputtering (Taylor et al., 2018), physical-vapor (Kim et al., 2022), chemical-vapor deposition

Received: September 15, 2023. **Revised:** January 9, 2024. **Accepted:** January 16, 2024

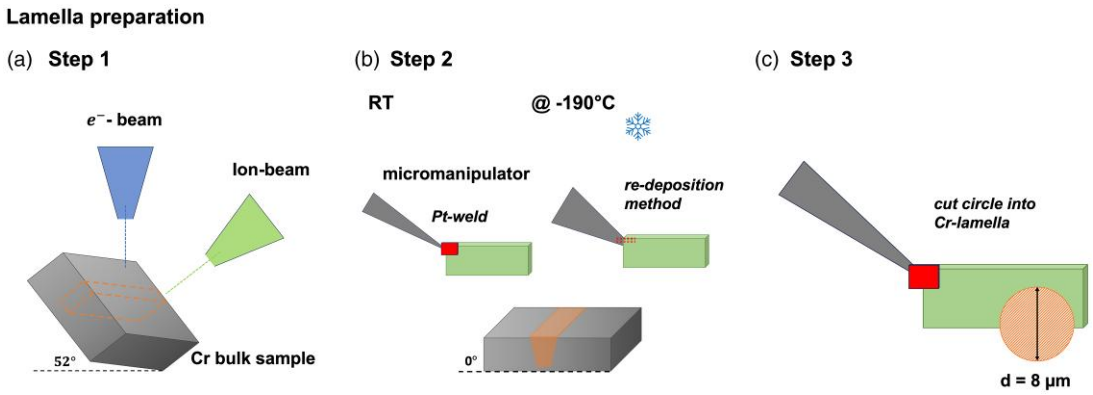

Fig. 1. Schematic view of the target preparation. (**a**) The trenches are cut at 52° and then (**b**) the lamella is attached to the micromanipulator at 0°, either at with the GIS or with the re-deposition, which is preferred at cryogenic temperature. (**c**) The opening with a diameter of 8 μm is then cut into the lamella.

(Felfer et al., 2014), or atomic-layer deposition (Li et al., 2021; Mosiman et al., 2021). Encapsulation of thin layers of liquid by using graphene conductive coating has also been proposed (Adineh et al., 2018; Exertier et al., 2021). These coatings were shown to lead to improvements in mass resolution and yield (Larson et al., 2013*a*, 2013*b*, 2013*c*), with the material used and the thickness of the coating influencing the electric field itself (Kellogg, 1982; Adineh et al., 2017). The improvement in yield has been posited to be due to pores being filled (Barroo et al., 2020), as these are known to result in early specimen fracture, likely due to stress concentration (Wilkes et al., 1972; Moy et al., 2011).

Coatings on flat substrates have also been used to encapsulate nanomaterials (Larson et al., 2015), including nanoparticles (Felfer et al., 2015; Josten & Felfer, 2022), nanowires (Prosa et al., 2008; Lim et al., 2020), or nanosheets (Kim et al., 2020) prior to performing the preparation of atom probe specimens. Shadowing effects during deposition, or the chemistry of the deposited material, i.e. the Pt-containing precursor in the FIB (Perea et al., 2017), or the use of an electrochemical potential that can affect the material to be deposited (Kim et al., 2018), can however make the analysis and interpretation arduous.

Recently, Woods et al. (2023) revisited an approach, first introduced by Kölling & Vandervorst (2009), to coat specimens directly *in situ* in the SEM-FIB, at cryogenic temperature. This method used material sputtered by the ion beam from the surface of a piece of metal placed in the vicinity of the already sharpened specimen. Douglas et al. (2023) also showed how this *in situ* deposition method could be used to strengthen the interface between a lift-out sample and the Si-support, which proved critical to the yield for specimens prepared at cryogenic temperatures. This approach allows for precisely controlling which section of the specimen's surface is coated and presents the advantage of being versatile with respect to the deposited material and the thickness of the coating.

Here, we report a more systematic study on the influence of these coatings on the final atom probe results. We demonstrate coating using Cr, Ti, Al, In, Bi, Co, and Ag on a Ga-FIB and/or a Xe-plasma FIB. The coating materials were deposited on a range of metallic and nonmetallic atom probe needles. We report on the composition and structure of the coating itself, and its multiple beneficial effects on the atom probe analysis, including increased yield, increased mass resolution, reduced background levels in laser pulsing mode, and an increased field of view. Ways forward with this approach are discussed for future possible generalization of the approach.

Methods

Materials

For this study, we selected a range of materials, which will be described in the relevant sections below. The targets used for *in situ* sputtering were typically small pieces of pure metals (99.99%) either sourced from Goodfellow, Fisher Scientific GmbH, or mixed leftover from the synthesis of larger ingots at the Max-Planck-Institut für Eisenforschung. The metal pieces were first cut into small $3 \times 7 \times 0.5$ mm pieces and then ground and polished to create a flat surface and remove any oxidation products. Afterwards, the metal pieces were mounted on a stub for SEM or the copper clip from Cameca Instrument Inc. The Fe-0.6 at%B-0.2 at%C thin films were prepared using physical-vapor deposition (BesTeck). The process involved co-sputtering from a pure iron target (99.995%, Mateck, Germany) and a boron target (99.9%, Kurt J. Lesker, USA) onto a MgO substrate. After sputter deposition, the thin films were annealed at 300°C for 40 h and then cooled to room temperature inside the vacuum chamber.

FIB-based Coating

To highlight the versatility of the approach, multiple SEM-FIBs were used to prepare specimens, a Helios 600i, a Helios 5 CX Ga SEM-FIB, and a Xe-plasma FIB-SEM Helios PFIB (all Thermo-Fischer Scientific, Hillsboro, OR, USA). The latter two instruments are equipped with EZLift tungsten micromanipulators, with the Helios 5 manipulator having cryogenic capabilities, whereas the 600i is equipped with an Omniprobe micromanipulator.

Figure 1 summarizes the lift-out procedure as described by Thompson et al. (2007): a lamella of the metal to be deposited, with typical size of $20 \times 10 \times 2$ μm, is lifted out and attached to the micromanipulator (step 1, Fig. 1a). This can be done either by welding using the gas injection systems (GIS) at room temperature or by redeposition under cryogenic temperatures (Schreiber et al., 2018; Woods et al., 2023) (step 2, Fig. 1b). A semi-circular opening with an 8–10 μm diameter is then cut into the lamella (step 3, Fig. 1c).

The steps for the coating of the needle-shape specimens are detailed in Figure 2. In the first step, in Figure 2a, the opening in the lamella is placed over a sharpened APT specimen, so that it is directly in the center of the opening as imaged by the ion beam (step 1). The distance between the bottom edge of the circle is typically about 1.5 μm from the specimen's tip.

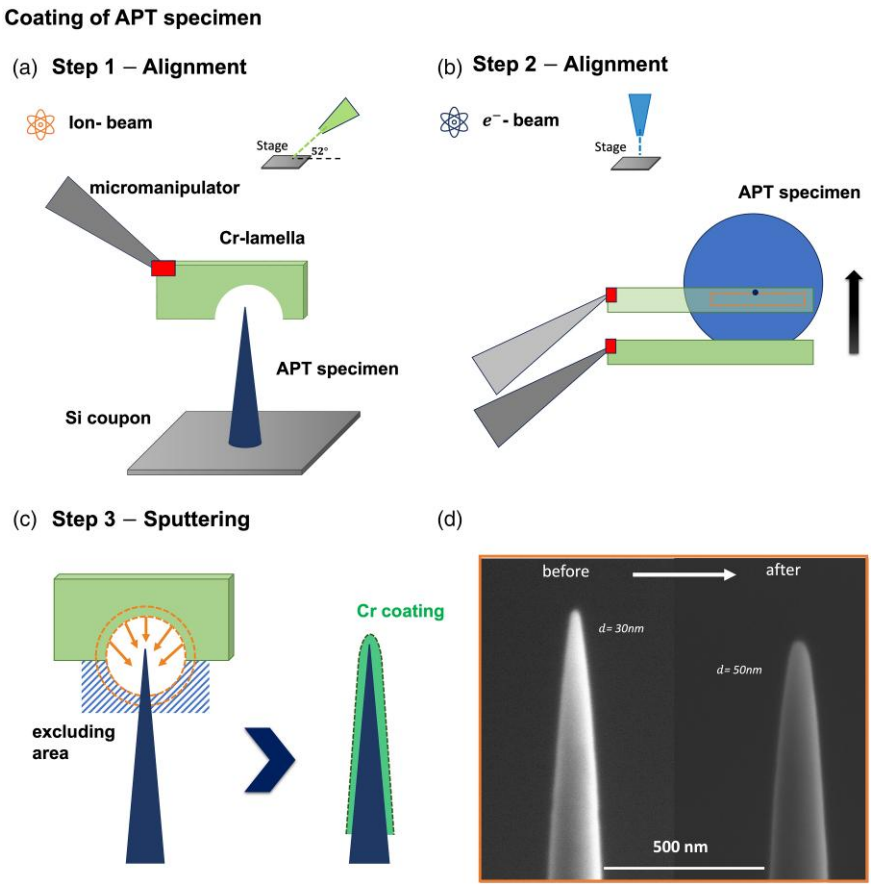

Fig. 2. Schematic of the different steps for *in situ* coating of specimens in the FIB. (**a**) Shows the positioning of the lamella in the ion beam in such a way that the specimen is in the center of the opening. (**b**) The alignment in the electron beam is shown, where the top view of the specimen is represented by the blue circle, while the arrow indicates the movement of the manipulator to bring the target to the desired position. (**c**) The ion beam is screened in the orange areas, while the blue area represents the exclusion zone. (**d**) SEM images before and after coating a Ni tip with Cr are shown.

The distance from the lamella to the tip and the diameter of the circle will determine the length of the specimen is coated. In the next step, in Figure 2b, the lamella is placed in the electron beam in such a way that the sharpened specimen is covered by the upper edge of the lamella (step 2). Finally, the ion beam is rastered on the metal target, from the inner circle outwards, using the pattern with the diameter of 12/8 μm and 1 μm in z-direction shown in orange in Figure 2c (step 3). To ensure that the ion beam does not hit and damage the specimen itself, an exclusion zone is added that covers the specimen, as indicated by the blue shaded area in Figure 2c.

Following a first deposition, the specimen stage is rotated by 90°, and a new layer is deposited. This process was repeated until a full 360° rotation was performed. Each side of the specimen was hence coated twice, which appeared to provide a sufficiently homogeneous and uniform coating for smooth atom probe analysis. Figure 2d shows an example of a Ni specimen, before and after coating with Cr. On this scale, the coating appears in the form of a homogeneous layer and indicated by a uniform increase in diameter of the specimen.

It is important to keep in mind that the parameters used depend on the material being sputtered and the desired film thickness. For Cr, sputtering was performed at 30 kV and 40 pA for 30 s. Note that the pattern settings are based on Thermofisher calculations for Si and are given in Supplementary Table S1. The parameters may vary using different instruments. The average time required to coat six samples from four sides is approx. 1 h, excluding preparation of the lamella.

In addition to coating needle-shaped samples, it is also possible to coat the surfaces of flat samples. Protection layers deposited using the Pt-precursor from the GIS are generally not perfectly dense and contain carbon residues from the precursor gas, which can then cause issues during imaging by transmission electron microscopy (TEM), and often make field evaporation in the APT of this layer problematic. When deposited with the ion beam, there can also be structural damage in the subsurface region (Thompson et al., 2007). With the method described in Figure 3, a metallic layer can be deposited *in situ* on the desired location of the sample's surface. The lamella is moved close to the surface and the ion beam is rastered over the rectangular area marked in orange, Figures 3a and 3b.

A higher-magnification SEM image shows a clear contrast between the deposited Cr layer and the underlying substrate, Figure 3c. The layer thickness is strongly dependent on the sputtering time. The lamella remains static in one position during sputtering as the coated area is significantly larger than the selected pattern due to the beam scattering. If a larger region of interest is required, the lamella can be moved, and the coating process repeated. The same parameters were used as for the needle-shaped specimen, but a longer deposition time of 1–4 min was required. In both cases, the coating can be done under cryo-conditions, making this method very versatile. Using the GIS under cryo-conditions is problematic because

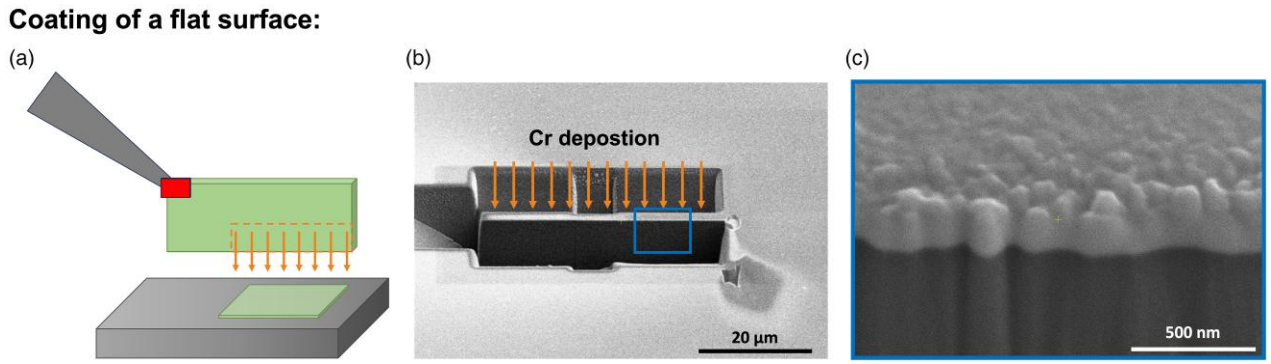

Fig. 3. (**a**) Schematic overview of the coating of a flat surface and in (**b**) the SEM image showing the coated surface. In (**c**), a SEM image with higher magnification contrast between Cr and the substrate is clearly visible.

the gas condenses on all cold surfaces, which makes a controlled deposition impossible. Using this method, a thin metal layer can be deposited under cryo-conditions in a controlled manner.

Atom Probe Tomography

Following preparation and coating, specimens were either transferred through air or via cryo/vacuum suitcase (Ferrovac) to a Cameca LEAP 5000 XS (straight flight path) or 5000 XR (reflectron) atom probe. The specific running conditions will be specified below for each set of results. Data reconstruction and analysis were performed using APSuite 6.3 software. The initial reconstruction was performed using the measured start radius and shank angle of the specimen obtained from the SEM image of the sharpened/coated specimen, following the point-projection protocol by Geiser et al. (2009). Where possible, the reconstruction parameters, image compression factor (ICF) and field factor (k_f) were calibrated using crystallographic poles as described in Gault et al. (2009) and adjusted to obtain lattice spacing reported in the literature.

(S)TEM

For the transmission electron microscope (TEM) analysis, a FEI Titan Themis microscope with an image corrector operated at 300 kV was used to reveal the structure of the *in situ* metallic coating of a Ni specimen. Energy-dispersive X-ray (EDX) analyses and high-angle annular dark field (HAADF) imaging was performed in scanning TEM (STEM) mode using the same instrument. For the 4D (S)TEM of the Fe(BC) specimen, a JEOL2200FS TEM was operated at 200 kV. EDX analyses and HAADF imaging were performed in STEM mode using the same instrument. Scanning Precession Electron Diffraction (SPED) (Harrison et al., 2022) was executed on the same TEM, with a measured beam size of ~1 nm and a 0.82° precession angle supplied by a Digistar hardware unit (NanoMEGAS SPRL). Each SPED dataset covered a scan frame comprising (255 × 276) pixels at a frame rate of 24 frames per second. Since the electron probe intensity distribution was strongly peaked, the datasets were indexed using an Automated Crystallographic Orientation Mapping (ACOM) tool.

Results and Discussion

Structure and Composition of the Coating

Specimens for APT were prepared using a Ga-FIB and a Xe-PFIB from nanocrystalline, high purity (99.99%) Ni. Through grinding of a Ni plate, which had been strongly deformed resulting in a nanocrystalline structure, specimens were prepared by FIB lift out, as outlined in Thompson et al. (2007). In addition, specimens were prepared from the B-doped Fe film (see Methods above). TEM and (S)TEM analyses were performed to study the structure and thickness of the deposited Cr layer deposited on pure Ni (fcc) and Fe (bcc).

Figure 4a displays TEM images after performing the sputter coating only once. A thin homogeneous layer has been deposited on the Ni specimen. After coating the specimen in each pass and rotating it 90° four times to coat it from all sides, the deposited layer thickness is approx. 10 nm. This is consistent with our estimation form the SEM images, shown in Figure 2. Interestingly, the Cr layer is conformal with the specimen, homogeneous and uniform over several hundred nanometers down the shank, as readily visible in Figure 4b. There seems to be no discernible shadowing effects or columnar growth of the sputtered layer, which have been previously reported in the literature (Prosa & Larson, 2017). EDX mapping in S(TEM) mode shows the Cr layer around the Ni needle (Fig. 4c).

Figure 4d is a close-up of a notch on the edge of the specimen. Following coating, the outer edge of the specimen is smooth and homogeneous, which is likely to reduce the stress localization, leading to increased mechanical stability of the specimen during analysis. However, it should be noted that the evaporation fields of the sample and the coating must be adjusted to avoid inhomogeneous evaporation (Larson et al., 2013*a*, 2013*b*, 2013*c*), which leads to locally stronger fields and thus possible higher stress between the coating and the sample. From the (S)TEM images, the sputtered Cr layer appears amorphous on the Ni specimen (Supplementary Fig. S1).

Figure 5a shows the HAADF-STEM images of the coated Fe-specimen from four sides. Figures 5b and 5c, are PED patterns pertaining to the crystal structure of Cr and obtained from different parts of the coating. ACOM-SPED indicates that the coating is nanocrystalline in part, with regions that could not be indexed and could be considered amorphous, Figure 5d. Due to the very close lattice constants of α-Cr and α-Fe, the indexing is not unambiguous and therefore has some inaccuracies. 4D-STEM data also collected from the same specimen allows to distinguish α-Cr and α-Fe through the specimen.

The results in Figures 4 and 5 suggest that the structure of the coated layer depends on the underlying substrate. If the lattice structures of the coating and the substrate are too

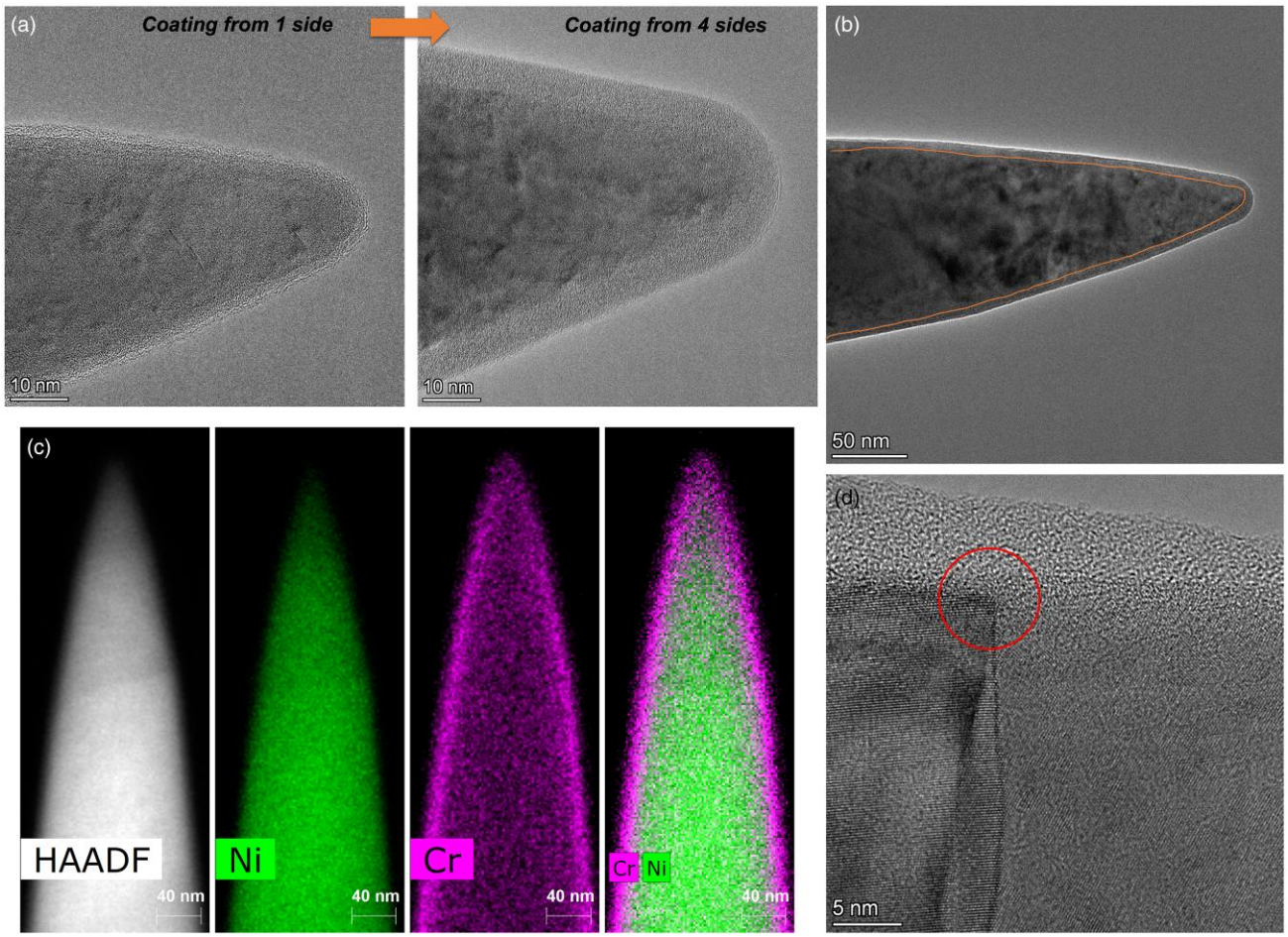

Fig. 4. (**a**) Shows a Cr coating on a Ni specimen from one side and from four sides for comparison. (**b**) Shows the tip with a homogeneous Cr layer of several hundred nanometers along the shaft of the tip with a coating thickness of approx. 10 nm. In (**c**), the EDX mapping shows the Cr coating around the Ni specimen. (**d**) Defects and roughness of the sample surface can be homogeneously coated, as shown here on the example of a grain boundary.

different, an amorphous layer will first form to compensate for the lattice mismatch between the two crystal structures. As the coating grows thick, and depending on the mismatch between the two crystal structures, the coating can become crystalline. Studies have shown that Cr grows amorphously on a glass substrate and has a crystalline structure on a crystalline substrate, supporting our observations on different substrate materials (Miller & Holland, 1997; Khanna et al., 2006). This can explain the amorphous Cr layer seen on Ni, and the nanocrystalline coating on Fe, on relatively thin coatings (10–20 nm).

From the perspective of the APT measurement, an amorphous layer may be preferable as they would leads to little or no stress on the sample's surface (Larson et al., 2013*a*, 2013*b*, 2013*c*), whereas nanocrystalline layers can exhibit heterogeneous field evaporation at defects of for different sets of atomic planes. From a heat conduction perspective, the opposite could be expected. It is possible that the structure depends not only on the substrate material but also on other parameters such as the use of Ga or Xe ions, ion beam acceleration voltage, and current. The deposition under cryogenic temperatures could also favor the amorphous formation of the Cr coating. All these parameters will be explored in future.

The chemical composition of the Cr coating depending on the use of a Xe and Ga-FIB on a Ni specimen was then analyzed by APT following transfer through ambient conditions to the atom probe. Figures 6a and 6b display a 10 nm slice of the reconstructions of specimens prepared by Xe-PFIB and Ga-FIB, respectively, at a chamber pressure of approx. $2.05{\cdot}10^{-6}$ mbar. The coating covers the top and sides of the specimen. The Xe and Ga distributions are visualized using isosurfaces. Xe tends to agglomerate, whereas Ga appears distributed across the entire Cr layer. The composition of the Cr layer varies strongly, with 55.01 ± 1.51 at.% Cr, 44.31 ± 1.59 at.% O and 0.68 ± 0.09 at.% Xe obtained on the PFIB (Table 1). This contrasts with the composition of the coating obtained by Ga-FIB that is 87.19 ± 1.40 at.% Cr, 7.36 ± 0.99 at.% O and 6.02 ± 1.46 at.% Ga (Table 1). Deposition of the Cr layer under cryogenic conditions on a Ga-FIB shows that the Ga implantation in the deposited layer is significantly lower by a factor of 3.12. The composition of the coating obtained in cryogenic condition is Ga-FIB that is 90.60 ± 0.66 at.% Cr, 7.47 ± 0.87 at.% O, and 1.93 ± 0.21 at.% Ga (Table 1). In contrast, the oxygen concentration in the Cr layer does not change much, while the pressure in the FIB is in the range of approx. $8.05{\cdot}10^{-7}$ mbar.

Oxygen likely originates from the fast formation of the passivating Cr-oxide in between two passes of the ion beam on the surface of the Cr lamella. The difference in composition could result from the fact that the Xe removes ions mostly from the surface, which is likely to be more enriched in oxygen. In general, a higher Ga content is observed compared to Xe, which can be attributed to its higher reactivity, deeper penetration,

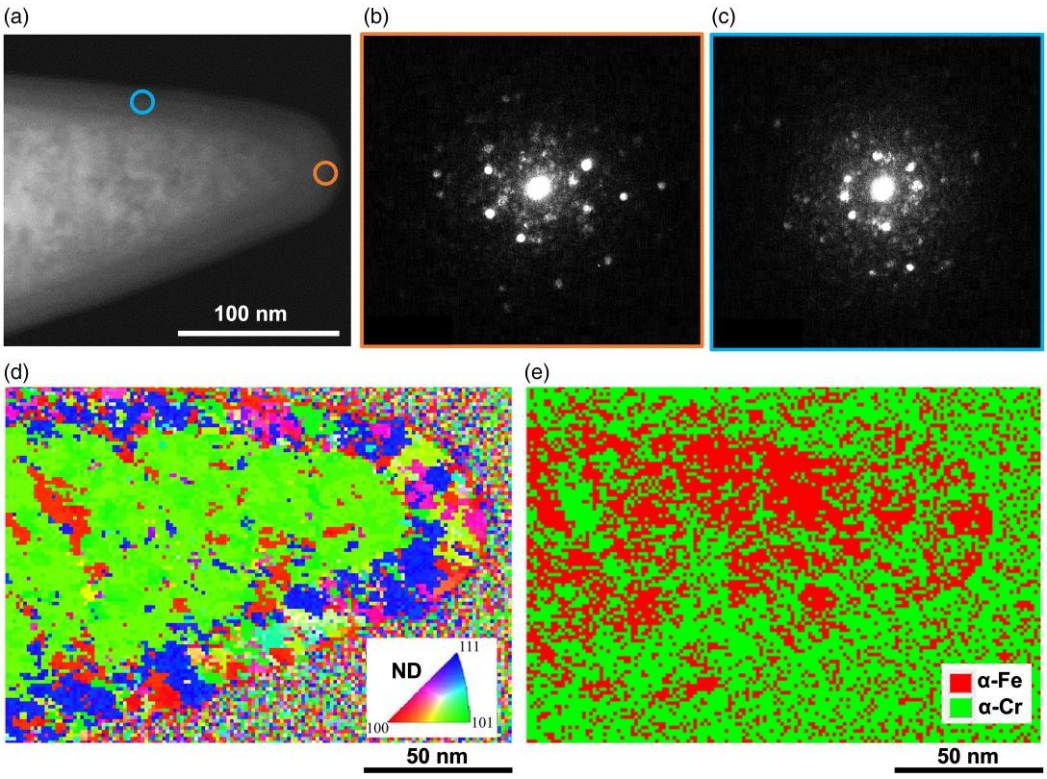

Fig. 5. (**a**) HAADF-STEM image of the Fe-1%B specimen after coating. (**b,c**) show the PED pattern from the orange and blue circle area and (**d**) visualizes the indexing of the 4D-STEM dataset. (**e**) Shows the phase detection of 4D-STEM datasets.

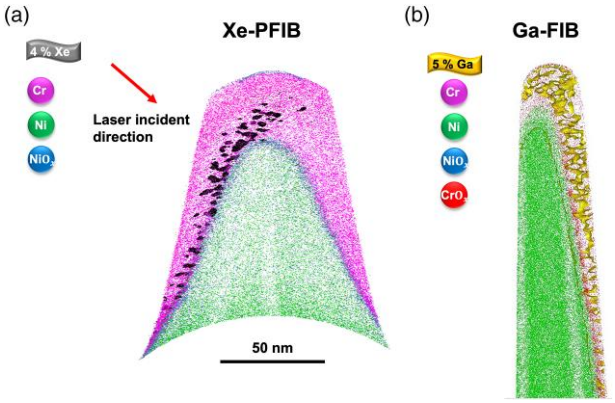

Fig. 6. Comparison of the structure of the Cr layer produced with a Xe and Ga-FIB. In (**a**), the Xe clusters with an isosurface concentration of 4 at % and in (**b**) the Ga distribution with an isosurface concentration of 5 at.% are visualized.

and overall higher concentration of Ga inside of the target material compared to Xe.

The use of Ga-FIB under cryogenic conditions significantly reduces the implantation of Ga, but it appears to have no significant effect on the oxygen concentration in the film from by sputtering from the cryogenically cooled Cr lamella. The oxygen concentration thus depends significantly on the formation of the oxide layer on the surface of the lamella, or at least the adsorption of O-containing species which can be facilitated at low temperature. These issues could be prevented by using an ultra-high-vacuum FIB.

An uneven distribution of Xe can be seen in the reconstruction (Fig. 6a). It has been shown in the TEM by Wittmaack & Oppolzer (2011) and in the APT studies by Estivill et al. (2016) of that Xe forms clusters in the substrate material during specimen preparation. The same phenomenon can be observed in the coated Cr layer by Xe ions. The nonuniform distribution of Xe clusters could be due to the position of the laser beam hitting the specimen (Fig. 6a). The relatively higher increase in the specimen temperature on that side, leading to slightly lower field enabling their field evaporation, whereas on the opposite side, preferential evaporation of Xe at the standing electrostatic field is more likely to occur.

Table 1. Average Composition of the Cr Coating Prepared by a Xe-PFIB (three specimens) and Ga-FIB at Room Temperature (five specimens) and Cryogenic Temperature (three specimens).

	Xe-PFIB	Ga-FIB	Cryo Ga-FIB
Ga	-	6.02 ± 1.46	1.93 ± 0.21
Xe	0.68 ± 0.09	-	-
Cr	55.01 ± 1.51	87.19 ± 1.40	90.60 ± 0.66
O	44.31 ± 1.59	7.36 ± 0.99	7.47 ± 0.87

All numbers are given in at.%.

Yield and Mechanical Resistance

Atom probe specimen from the same nanocrystalline Ni was prepared and Cr-coated using a Ga-FIB (Helios 5 CX). APT analyses were performed on a LEAP 5000 XS at 50 K, in laser pulsing mode (laser pulse energy of 40 pJ), with a repetition rate of 200 kHz and with a target detection rate of 1.5 ion per 100 pulses, on average, for both uncoated and Cr-coated specimens. Four uncoated Ni specimens were analyzed. The voltage curve from one is plotted in Figure 7a. It exhibits

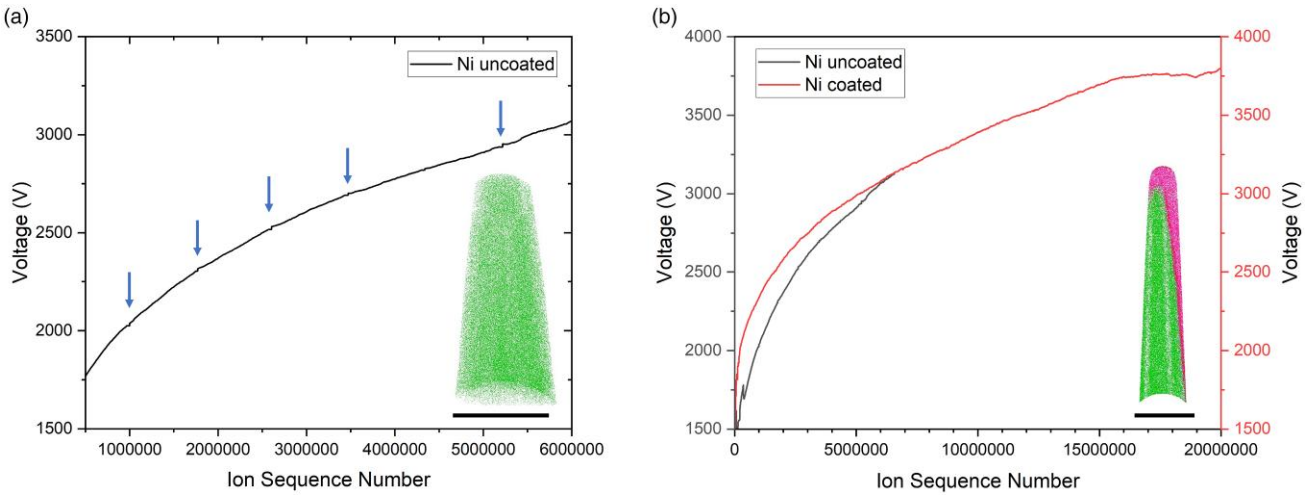

Fig. 7. In (**a**), the voltage curve for the uncoated Ni sample shows several dips, indicating structural changes during the measurement due to GB or other defects and inhomogeneities. (**b**) Compares the voltage curve for the uncoated and coated Ni samples, showing a monotonous increase for the coated sample with no noticeable dips.

multiple dips, marked with blue arrows in Figure 7a, that are related to grain boundaries as proven by detector hit maps, shown in Supplementary Figures S2a–S2c. These dips do not correlate with any detectable changes in the evaporation rate (Supplementary Fig. S2d), or specimen fracture (Gault et al., 2012*a*, 2012*b*). In each case, the specimen fractured before 6 million ions could be collected. After coating the nanocrystalline Ni specimen, the voltage dips are no longer observed, as can be seen from the voltage curve in Figure 7b. For three analyzed Cr-coated specimens, the analysis was stopped when a set voltage of 8 kV was reached, and for each dataset, 60–100 million ions were collected without specimen fracture occurring.

We attribute this increase in yield and sample throughput to more stable field evaporation conditions. The high density of grain boundaries in nanocrystalline materials makes them particularly susceptible to fracture. The Cr coating appears to smooth the surface roughness out, and fill in some of the notches or pores, as observed by TEM in Figure 4d, thereby explaining the improved field evaporation conditions. Mechanical stabilization and the associated improvement in yield and throughput of coated samples were observed for the measurement of nanocrystalline Ni here and for a range of different material systems (Singh et al., 2023; Woods et al., 2023), which is in agreement with previous work (Kölling & Vandervorst, 2009; Larson et al., 2013*a*, 2013*b*, 2013*c*).

Mass Spectrum Improvements

Improvement in the mass resolution and background levels with a thin metallic coating of poor thermally conducting specimen have previously been reported (Larson et al., 2013*a*, 2013*b*, 2013*c*; Seol et al., 2016). Here, a small fragment from the dentin of a tooth of an unidentified dinosaur, found in South Korea, was analyzed by APT on a LEAP 5000 XR. APT analyses were performed at 50 K, in laser pulsing mode (laser pulse energy of 60 pJ), with a repetition rate of 100 kHz and with a target detection rate of 1.0 ion per 100 pulses, on average, for both an uncoated specimen and a Cr-coated specimen. Specimens were prepared on a Ga-FIB (Helios 600i) using the protocol in Thompson et al. (2007).

Biominerals, such as teeth, consist mainly of hydroxyapatite where Ca is the main constituent, along with other inorganic elements (Mg, Zn, P, …). They typically have poor thermal diffusivity, and therefore tend to form more pronounced thermal tails during APT analysis (Gordon & Joester, 2011; Gordon et al., 2012). In addition, these materials have poor absorption properties for the laser, so that a higher laser pulse energy is required to obtain field evaporation under electrostatic field condition that do not lead to appreciable background levels. The tails of the mass peaks lead to a loss of information, particularly for impurities and trace elements that may be indistinguishable below the thermal tails.

To investigate the influence of the Cr coating on improving thermal conductivity, some dentin samples were coated with Cr and others were not. Figure 8 shows a section of the mass spectrum obtained from the analysis of a non-coated sample (blue) with over 11 million ions, and a coated sample (red) with over 21 million ions. Both spectra have been normalized to the $^{40}Ca^{2+}$ peak at 20 Da.

In the uncoated samples, the long thermal tail of the $^{40}Ca^{2+}$ peak leads to a considerable overlap with the peaks of the other Ca isotopes. The thermal tailing spreads over a long area, indicating poor thermal conductivity of the material. Such long tailings can make the identification and quantification of trace elements impossible. It is also difficult to identify isotope ratios, which can be critical in quantifying data when there are overlapping peaks and for the dating of fossils and minerals (Reddy et al., 2020). The shape of the Ca peak is typical for (bio)minerals obtained from a different biominerals in the literature (Grandfield et al., 2022).

In the case of the Cr-coated specimen, the mass resolution is vastly improved by reducing the thermal tailing, which greatly simplified the peak identification and separation between signals. This facilitates the detection or quantification of peaks in the thermal tailing, e.g. $^{31}P^{2+}$ at 15.5 Da, which were not possible to detect without Cr coating. In addition, more accurate isotopic ratio measurements are possible: for the uncoated specimen the $^{40}Ca^{2+}$ peak represents only less than 72 at.%, whereas it is 94.9 at.% for the coated specimen, noting that

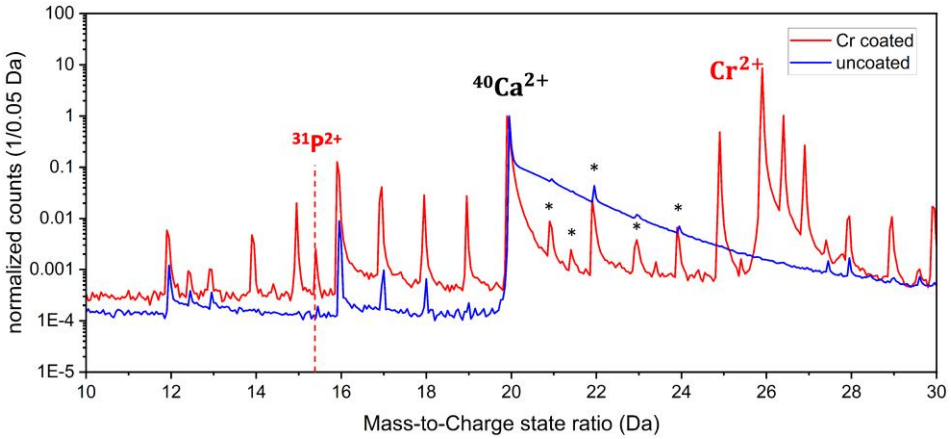

Fig. 8. Normalized mass spectra to the Ca peak for a coated (red) specimen and uncoated (blue) specimen prepared from the dentin of a fragment of an unidentified dinosaur tooth. An asterisk indicates the different isotopes of Ca.

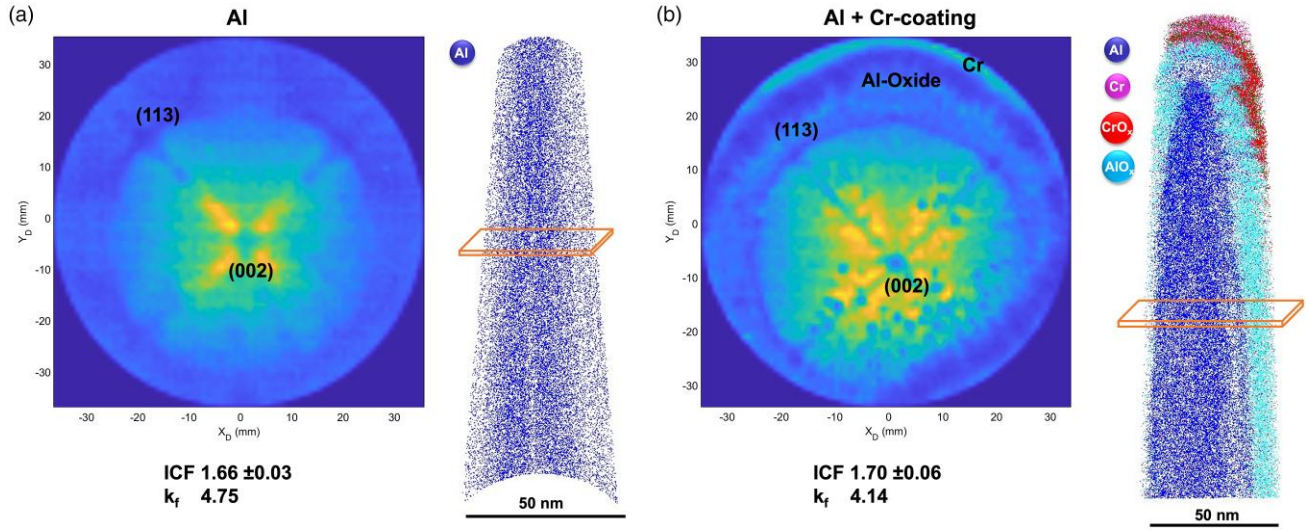

Fig. 9. (**a**) Data for the uncoated Al specimen clearly shows the (002) and (113) poles in the detector hit maps, along with the 3D reconstruction. (**b**) The Cr-coated Al specimen shows the same poles in the Al core, and the passivating surface oxides around the specimen indicate a larger field of view. The extracted area for the desorption map is marked with an orange parallelepiped.

the natural abundance is 96.9 at.%. With the Cr coating, it is also possible to detect other low abundance isotopes of Ca, whereby it should be mentioned that the peak at 23 Da has an overlap with $^{23}Na^{+}$ and is therefore higher.

We did not perform specific quantification of the improvement in mass resolution or background level since the specimen geometry (radius, shank angle, length) varies from specimen to specimen, even over the course of a single analysis. The change in shank angle alone affects substantially the mass resolution of the atom probe data, as demonstrated experimentally and computationally by Perea et al. (2008).

Effect on the Field-of-View: Analysis of Aluminum

Pure-Al Analyses

Next, we wanted to investigate the effect on the field-of-view (FoV) and possible changes in the ICF. Specimens were prepared from a pure Al plate, ground, and polished to remove surface oxides, using the Xe-PFIB to minimize any spurious effect of Ga implantation on the visibility of crystallographic poles. To accurately determine the change in ICF and FoV, while avoiding the influence of different radii or shank angles from specimen to specimen, we first measured 8 million ions from a specimen, then performed the Cr coating and measured the same specimen again. The APT analyses were performed on a LEAP 5000 XS at 50 K, in laser pulsing mode (laser pulse energy of 40 pJ), with a repetition rate of 200 kHz and a target detection rate of 1.5 ions per 100 pulses, on average. The same parameters were used for the uncoated and Cr-coated samples to aim for consistent measurement conditions. Figures 9a and 9b report on data obtained on the pure Al specimen before and after coating, respectively. Since the specimen transfer from the atom probe into the FIB was done in ambient atmospheric condition, a thin oxide layer has formed, as visible in Figure 9b. Similar results were obtained for three uncoated, and later coated, specimens.

To study a native oxide on an APT sample, it is necessary to capture the first thousands of atoms from the tip apex. This can be very challenging due to alignment requirements and due to their tendency to fracture off prior to reaching the metal/oxide interface. Here, after Cr coating, the native oxide layer on the tip apex and along the shank of the specimen

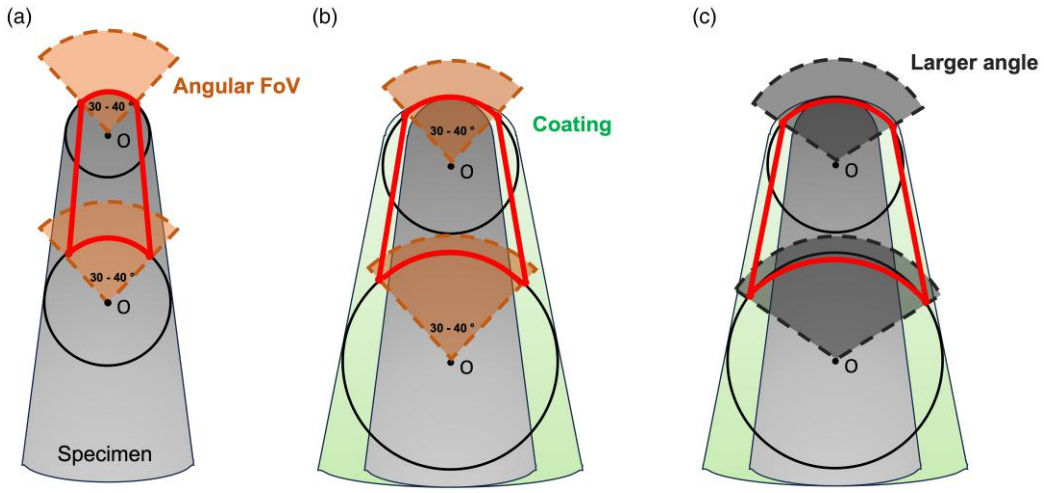

Fig. 10. (**a**) Schematic view of the angular FoV of an uncoated sample, in red is delineated the analyzed volume by APT. (**b**) The coating makes the specimen thicker, thereby increasing the imaged surface area at the specimen's tip, even with a constant angular compression. (**c**) A larger angular FoV arising from a change in the ICF would simply make the FoV mildly wider.

can be analyzed, leading to a massive increase in square nanometers of analyzable oxide/metal interface data. The capability of studying the surface of the atom probe tip is significant for any research group studying surface catalytic or oxidation and could lead to a higher success rate and throughput in the future. The thickness of the natural oxide layer on Al was measured based on the APT analysis to be between 6 and 8 nm, which is in good agreement with literature values (Evertsson et al., 2015).

Effect on the Reconstruction Parameters

Detector hit maps from the analysis of the specimen prior to coating, and after the coating, show clear crystallographic poles, Figures 9a and 9b, respectively. The ICF depends on the theoretical and observed crystallographic angles between two poles (Gault et al., 2008). Poles pertaining to the (002) and the four variants of the (113) planes were used to calculate the ICF, which is 1.66 ± 0.03 and a calculated k_f of 4.75 following calibration. After coating the same specimen with Cr, Figure 8b, the ICF was calculated using the same poles when visible, and it was 1.70 ± 0.06, with a k_f of 4.14 determined from adjusting the (002) plane spacing at a depth of approx. 150 nm into the Al.

The field evaporation of the surface atoms results in a progressive increase in the tip's radius that typically results in a decrease in k_f and ICF (Gault et al., 2011; Loi et al., 2013). Here, the decrease in k_f can be explained by the increase in the specimen's radius due to the coating (Gault et al., 2011; Loi et al., 2013). However, contrary to the expectation that the ICF should drop with increasing radius (Gault et al., 2011; Loi et al., 2013), we see no significant change in the ICF after the Cr coating has been evaporated from the top and the Al core is being analyzed—maybe a slight additional compression of the field lines and therefore of the ion trajectories arising from the presence of the Cr coating, but no severe distortions toward the interface between the metal and the coating.

Origins of the Increased Field-of-View

A striking difference following coating is the analysis of the native oxide on the specimen's shank, which indicates a significant increase in the imaged surface area at the specimen, despite a limited change in angular compression, i.e. the ICF is almost constant, as illustrated in Figure 10. There are two important factors here. First is the angular field-of-view, that is typically between ±25 and 30° about the specimen's main axis, and that relates to the angular compression of the trajectory reflected by the ICF (De Geuser & Gault, 2017). Second, this angular FoV defines the actual FoV that is the imaged area at the specimen's surface shown by the red arc in Figure 10a, and that corresponds to the reverse projection of the detector onto the emitting specimen. As the radius increases because of the field evaporation during the APT analysis, the imaged surface area also increases, leading to a total analyzed volume delineated by the thick red lines.

Coating the specimen is equivalent to increasing its radius. Even if the angular FoV (i.e., ICF) remains the same, as in Figure 10b, the imaged surface area increases, allowing for imaging the sides of the original specimen. A similar increase in the imaged surface could arise from an increased angular FoV, Figure 10c, yet this would have translated into a strong change in ICF, which was not measured experimentally here, but had been reported previously (Du et al., 2013). Possible changes in the thickness of the coated film would primarily lead to changes in the specimen's end radius, leading to changes in the voltage to reach the electrostatic field necessary to reach the set detection rate, and not much on the compression of the ion trajectories, as suggested by Figure 10b. Measurable changes in the voltage were not observed experimentally, suggesting a rather conformal and homogenous coating. The application of this thin coating appears to lead to an increased FoV similar to the use of an electrostatic lensing system (Bostel & Yavor, 2010; Tegg et al., 2023). The use of the conventional reconstruction algorithm did not lead to severe distortions on the edges of the FoV.

Effect on the Field-of-View: Precipitates in Al-Alloy

To demonstrate the influence of the change in the FoV, a similar set of analyses on an Al-5.18Mg-6.79Li (at.%) alloy aged for 8 h at 150°C to form spherical δ′-precipitates, for more details, please refer to Gault et al., 2012*a*, 2012*b*. Following grinding and polishing to remove surface oxides, specimens were prepared using the Xe-PFIB. APT analyses were

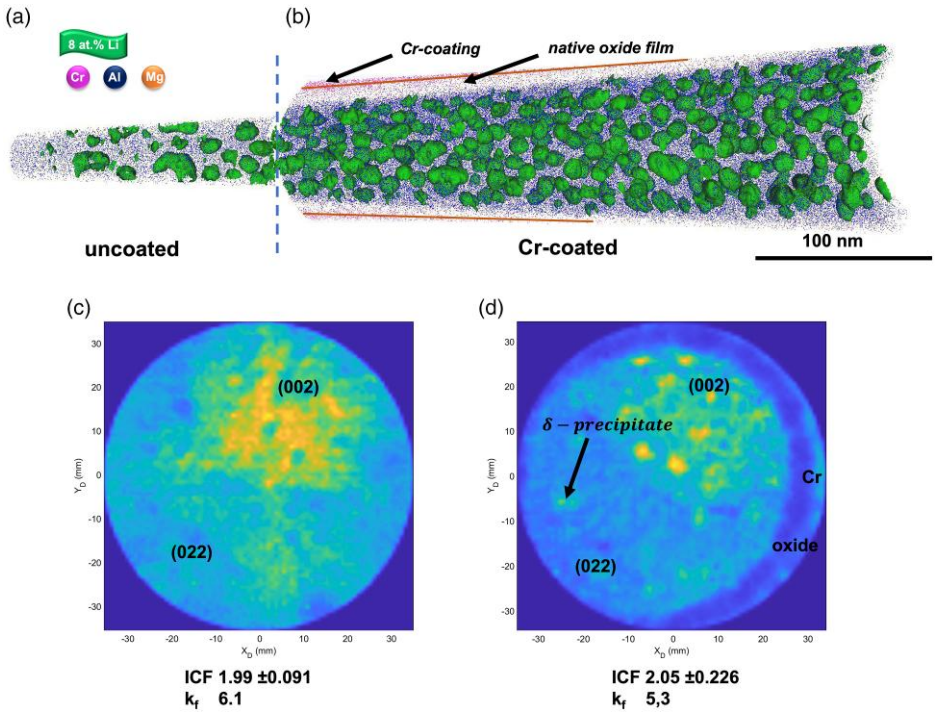

Fig. 11. In (**a**) a comparison between uncoated and coated samples, Li δ′-precipitates are visualized using an isosurface concentration of 8 at.% Li. In the Cr-coated sample (**b**), the Cr layer and the naturally formed oxide layer can be seen, the interface between the two being highlighted by orange lines. (**c,d**) Show the corresponding desorption maps for the coated and uncoated specimens.

performed on a LEAP 5000 XS at 50 K, in laser pulsing mode (laser pulse energy of 20 pJ), with a repetition rate of 200 kHz and a target detection rate of 1 ion per 100 pulses, on average, for both the uncoated and Cr-coated samples.

Figure 11 shows a 10 nm thick slice through the combined reconstructions obtained from the analysis of the same specimen uncoated (Fig. 11a) and Cr-coated (Fig. 11b). The ICF was determined using the two poles marked in Figures 11c and 11d, and the k_f factor was calculated by adjusting the spacing of the (002) planes. Like the pure Al specimen discussed above, no significant change in the ICF is observed. The increase in field-of-view offered by the Cr coating allows for imaging the native oxide and part of the Cr layer itself, with the Cr/native oxide interface indicated by orange lines. It also leads to a substantial increase in the number of precipitates imaged through the specimen's cross-section. This increase in the number of analyzed precipitates for a single specimen in one measurement can help improve statistical accuracy, and it is also possible to analyze larger precipitates that may not be directly in the center of the sample. These were also highlighted as advantages arising from the use of the lensing system in other instrument design (Bostel & Yavor, 2010; Tegg et al., 2023), but the same effect can be achieved by the thin metallic coating of the specimen using a conventional atom probe geometry.

Discussion

Perspective on the Benefits of Coatings

Several effects of an *in situ* deposited metallic coating on APT specimens were reported, including improved mechanical resistance, better thermal conductivity, and an increase in the FoV. It is interesting to note that the ICF does not change significantly, indicating only a small additional compression of the field lines. A major advantage of this method is that no additional instrumentation is required, and the coating can be deposited in any FIB, with a Ga or Xe source and under cryogenic conditions.

In addition, the coating of the samples allows the complete oxide layer around the tip to be seen, as well as the Cr layer, thus allowing the outer layer and the thickness of the oxide layer to be analyzed. In the recently released Invizo instrument, an electrostatic lensing system compresses the trajectory of the ions to increase the FoV up to 90–100%. Tegg et al. (2023) reported the analysis of the outer oxide layer formed on a Zr specimens, however, as full cross-section of the specimen cannot be imaged, the outermost part of the oxide in contact with the environment is not analyzed over the full length of the specimen, hindering the analysis of the oxide layer through it full thickness. To confirm that the entire specimen's cross-section was analyzed often requires the use of microstructural features at the periphery of the specimen imaged by correlative electron microscopy (Diercks et al., 2013). These can introduce structural damage from electron bombardment and lower the yield of atom probe measurements (Herbig & Kumar, 2021). In contrast, the coating acts as a clear marker to identify the original specimen, including its native oxide layer.

It was also reported that the lensing system used to increase the FoV in the Invizo instrument leads to severe distortions in the reconstruction (Tegg et al., 2023). These are related to strong compression of the field lines and trajectories that are not appropriately taken into consideration in the currently available algorithms based on a point-projection model, making accurate reconstruction difficult. Cr coating does not lead to a significant change in the compression, meaning that current reconstruction algorithms remain applicable, and no noticeable change or distortions of the spherical δ′-precipitates can be observed in Figure 11.

Limitation

The coating is sometimes imaged only on one side, as in Figure 9b. This could be related to a slight tilt of the specimen's main axis with respect to the microscope's optical axis, or to a misalignment of the specimen with respected to the local electrode or the detector. In this case, the estimated ICF appears to be higher by 6% between the (002) and (113) poles marked in the figure, compared to between the (002) and the two (113) poles located on the perpendicular zone axis. Differences in the compression for specimen that do not exhibit cylindrical symmetry had previously been reported (Larson et al., 1999), which would lead to slight distortions in the reconstructed data since a single ICF is assumed across the FoV. This does not appear to be related to the location where the laser hits the specimen (bottom left in the detector hit map). The presence of a thicker coating on one side could be due to a slight misalignment during the deposition process, or the specimen bending slightly, as was sometimes observed when the shank angle is too low and/or radius of the specimens is too small (see Supplementary Fig. S3 for Al). This explains that the apparent change in the FoV between the datasets in Figures 9a and 9b is related to the fact that, after coating, the imaged cross-section is only on one the side of the original specimen, as illustrated in Supplementary Figure S4.

From the detector hit maps of the coated specimen (Fig. 9b), many areas of higher and lower event density appear, forming a speckled pattern indicative of overheating of the specimen from the laser. This observation suggests that the absorption of laser energy by Cr in the UV region is significantly higher than that of pure Al. Therefore, more energy is absorbed in the form of thermal energy which heats the Al sample significantly (Vurpillot et al., 2009). Several publications have reported that Cr exhibits photoexcitation, which contribute to the higher sample temperature (Al-Kuhaili & Durrani, 2007; Khalaf et al., 2021). The presence of the oxide layer around the Al and the multiple interfaces can also limit the heat flows away from the apex. However, the higher absorption of the Cr layer can also be a great advantage for materials that have very poor absorption properties for the laser at the used wavelength (here, $\lambda = 355$ nm), such as glass (Kellogg, 1982) or (bio)minerals (Reddy et al., 2020; Grandfield et al., 2022), or most metals at shorter wavelengths. This would allow significantly lower laser energies to be used, reducing the base voltage, and extending the lifetime of the samples, along with reducing thermal tailing.

In addition, there can also be severe interference in the mass spectrum between peaks from the materials being analyzed, the coated metal and its possible oxides—the APT analysis of Cr oxides shows many series of peaks up to relatively high mass-to-charge state ratios (La Fontaine et al., 2015). It is therefore important to select the coating material in such a way that the expected signals from both the analyzed material and the coating material do not severely overlap in the mass spectrum. The interference between signals from the coating and the material of interest is readily visible in Figure 8. To avoid misinterpretation, it is often simpler to extract the inner part of the dataset into a separate reconstruction in the analysis software by selecting the appropriate region of the voltage curve and detector region-of-interest or extracting from a Cr-isosurface for instance and reassigning the peaks in the mass spectrum. At this stage, it is unclear whether the sputtered metal reacts with the surface of the original specimen or its native oxide, or if the deposition process causes structural damage or implantation subsurface. This will be studied in future work.

Future Considerations

Our coating approach is versatile, and many parameters can be optimized. For example, the coated metal can be chosen to match the evaporation field of the coated material to minimize the evaporation field contrast and possible resulting aberrations.

There are many possibilities for the metal to be coated, and it is easy to change the target, but the deposited metal must adhere sufficiently and not react with the incident ion beam. In this respect, the choice of an element with only one or two isotopes, with relatively well-defined oxides, or with a low tendency to form oxides, or with high atomic masses, may seem optimal. Noble metals such as Ag, Pt, Pd, or Au could also avoid possible reactions with the surface.

For each material, suitable sputtering parameters must first be found and optimized in the FIB, but this process offers the possibility of using a wide range of metals. Ti, In, Bi, Al, Co, and Ag have also been tried out with similar deposition parameters (see Supplementary Figs. S5–S10).

The Ag layer was very inhomogeneous and will require future optimization. Nevertheless, the mass spectrum of the Ag coating layer shows promising behavior, with only Ga and two unidentified peaks appearing at lower mass-to-charge state ratios than Ag. At higher masses, several Ag oxide peaks appear, which may also be related to the speckled texture and its nonuniform evaporation behavior (Supplementary Fig. S6). For In, the reaction with the incident Ga ions from the primary beam resulted in an uneven deposition from a possibly liquid source, as the In-Ga alloy (42.6 (In)/52.4 (Ga) at.%) system (Anderson & Ansara, 1991) has a low temperature eutectic (see Supplementary Fig. S7). This could be optimized by using the Xe-PFIB.

Similar observations were made for Al coated on a biomineral, where the Ga content in the sputtered layer was approx. 2.17 ± 0.33 at.%, but the deposited layer was very homogeneous and uniform. This effect could be avoided by using Xe-PFIB, whereas Al is a promising candidate as a low evaporation material for coatings (Supplementary Fig. S5). Only two candidates that have so far shown good sputtering properties with the same parameters are Ti, which has five isotopes and is therefore not perfect choice (Supplementary Fig. S10), due to the high probability of overlap and the formation of oxides, which further complicate the mass spectrum. The second candidate is Co, which also forms a uniform layer and has only one isotope, which makes Co attractive for a coating material, because the probability for an overlap is lower. There remains a possibility that Co overlaps with some peaks of interest, and a single isotope may prevent decomposition and improvement in the composition measurement. However, Co has a higher evaporation field than all the other materials used in these studies, which needs to be considered when choosing the coating material (Supplementary Fig. S9).

The energy distribution of the deposited atoms or secondary ions emitted by the target is primarily undetermined at this stage, and so is how these ions possibly affect the specimen's surface upon deposition—i.e. causing implantation or structural damage to the surface and subsurface layers. Adjusting the energy of the primary Ga or Xe beam may be a lever to adjust this, to minimize damage from these secondary particles.

Finally, previous studies have suggested that a coated layer can be used to increase the electrical conductivity of the

specimen, allowing the measurement of insulators in voltage-pulsing mode (Adineh et al., 2016, 2017, 2018). An improved electrical conductivity of the samples can be seen in Supplementary Figure S5. Prior to the coating, a clear charging effect can be observed due to the poor electrical conductivity of the specimen in the electron beam, which disappears after the Cr coating, indicating charge transport to the shank of the specimen. The effect of these coatings on electrical and thermal conductivity provides the motivation to carry out simulations in the future to understand their effect.

Here, we only used laser-pulsed atom probe, which has more parameters to be adjusted (wavelength, laser energy, frequency) to optimize the chemical composition (Mancini et al., 2014). In addition, the increase in temperature can lead to diffusion processes on the surface, which have a negative effect on the accuracy of the reconstruction and thus lead to artifacts (Larson et al., 2013*a*, 2013*b*, 2013*c*; Lefebvre-Ulrikson et al., 2016). On the opposite side of the laser incident, a "shadow effect" occurs. This reduces the mass resolution of the APT, especially for materials with poor thermal conductivity (Sha et al., 2008). Coating poorly conducting materials with a metallic layer and measuring in voltage mode would be an interesting approach to avoid the negative effects of using thermally induced field evaporation. The field evaporation contrast may lead to a buildup of stresses at the interface between the specimen and the coating and facilitate fracture, or simply create additional aberrations, which motivates further studies.

Summary and Conclusions

To summarize, we have demonstrated a low-cost and fast method to form a conformal coating on APT specimens that appears homogeneous and uniform. The method uses *in situ* sputtering of a metallic target by the FIB. This approach is versatile and leads to many benefits including:

(i) environmental protection during transfer between the FIB and the atom probe, which is critical for studies of e.g. surfaces and reactive materials;
(ii) a higher sample yield, possibly due to the mechanical stabilization provided by the coating;
(iii) improved mass resolution and background level leading to improved sensitivity by a better thermal conductivity of and or better absorption of the laser energy by the metallic coating;
(iv) possibilities to image the shank of the specimens, which dramatically increases the surface area of e.g. native oxides formed on atom probe specimens and further stabilization of the oxide layer evaporation;
(v) the possibility to detect larger numbers of precipitates due to a larger field of view within the same specimen, thus increasing the throughput and statistical power and decreasing the number of runs and lower the cost; and
(vi) increasing the field of view by increasing the radius of the original tip does not compress the field lines, so the existing reconstruction algorithm is retained.

Much remains to be explored, such as optimizing the sputtering parameters and their influence on the thickness or crystalline structure of the coating, adapting the sputtering parameters to different target materials, the influence of the coating on nonconductive or poorly thermally conductive materials, or the influence of the electrical and thermal conductivity of the target metal on analytical performance.

Availability of Data and Materials

The authors have declared that no datasets apply for this piece.

Supplementary Material

To view supplementary material for this article, please visit https://doi.org/10.1093/mam/ozae006.

Acknowledgments

We thank Uwe Tezins, Andreas Sturm, and Christian Broß for their support at the FIB & APT facilities at Max-Planck-Institut für Eisenforschung GmbH.

Financial Support

T.M.S., I.M., E.W., and B.G. are grateful for funding from the DFG through the award of the Leibniz Prize 2020. I.M., E.W., and B.G. are grateful for funding from the ERC—SHINE (771602). M.K. and B.G. acknowledge financial support from the German Research Foundation (DFG) through DIP project no. 450800666. X.C. is funded from DFG project ID 405553726-TRR 270, project Z01. C.J. is grateful for financial support from Alexander von Humboldt Foundation. K.J. is grateful for funding from the Samsung Electro-Mechanics. S.-H.K. acknowledges the KIAT grant funded by the Korea Government MOTIE (P0023676).

Conflict of Interest

The authors declare that they have no competing interest.

References

Adineh VR, Marceau RKW, Chen Y, Si KJ, Velkov T, Cheng W, Li J & Fu J (2017). Pulsed-voltage atom probe tomography of low conductivity and insulator materials by application of ultrathin metallic coating on nanoscale specimen geometry. *Ultramicroscopy* **181**, 150–159. https://doi.org/10.1016/j.ultramic.2017.05.002

Adineh VR, Marceau RKW, Velkov T, Li J & Fu J (2016). Near-atomic three-dimensional mapping for site-specific chemistry of 'superbugs'. *Nano Lett* **16**, 7113–7120. https://doi.org/10.1021/acs.nanolett.6b03409

Adineh VR, Zheng C, Zhang Q, Marceau RKW, Liu B, Chen Y, Si KJ, Weyland M, Velkov T, Cheng W, Li J & Fu J (2018). Graphene-enhanced 3D chemical mapping of biological specimens at near-atomic resolution. *Adv Funct Mater* **28**, 1801439. https://doi.org/10.1002/adfm.201801439

Al-Kuhaili MF & Durrani SMA (2007). Optical properties of chromium oxide thin films deposited by electron-beam evaporation. *Opt Mater* **29**, 709–713. https://doi.org/10.1016/j.optmat.2005.11.020

Anderson TJ & Ansara I (1991). The Ga-In (gallium-indium) system. *J Phase Equilibria* **12**, 64–72. https://doi.org/10.1007/BF02663677

Anway AR (2003). Field ionization of water. *J Chem Phys* **50**, 2012–2021. https://doi.org/10.1063/1.1671324

Balogh Z, Reda Chellali M, Greiwe G-H, Schmitz G & Erdélyi Z (2011). Interface sharpening in miscible Ni/Cu multilayers studied by atom probe tomography. *Appl Phys Lett* **99**, 181902. https://doi.org/10.1063/1.3658390

Barroo C, Akey AJ & Bell DC (2020). Aggregated nanoparticles: Sample preparation and analysis by atom probe tomography.

Ultramicroscopy **218**, 113082. https://doi.org/10.1016/j.ultramic.2020.113082

Bostel A & Yavor M (2010). (12) Patent Application Publication (10) Pub. No.: US 2010/0223698 A1. 1.

Bunton JH, Olson JD, Lenz DR & Kelly TF (2007). Advances in pulsed-laser atom probe: Instrument and specimen design for optimum performance. *Microsc Microanal* **13**, 418–427. https://doi.org/10.1017/S1431927607070869

Cerezo A, Warren PJ & Smith GDW (1999). Some aspects of image projection in the field-ion microscope. *Ultramicroscopy* **79**, 251–257. https://doi.org/10.1016/S0304-3991(99)00071-6

De Geuser F & Gault B (2017). Reflections on the projection of ions in atom probe tomography. *Microsc Microanal* **23**, 238–246. https://doi.org/10.1017/S1431927616012721

Diercks DR, Gorman BP, Kirchhofer R, Sanford N, Bertness K & Brubaker M (2013). Atom probe tomography evaporation behavior of C-axis GaN nanowires: Crystallographic, stoichiometric, and detection efficiency aspects. *J Appl Phys* **114**, 184903. https://doi.org/10.1063/1.4830023

Douglas JO, Conroy M, Giuliani F & Gault B (2023). In situ sputtering from the micromanipulator to enable cryogenic preparation of specimens for atom probe tomography by focused-ion beam. *Microsc Microanal* **29**, 1009–1017. https://doi.org/10.1093/micmic/ozad020

Du S, Burgess T, Tjing Loi S, Gault B, Gao Q, Bao P, Li L, Cui X, Kong Yeoh W, Hoe Tan H, Jagadish C, Ringer SP & Zheng R (2013). Full tip imaging in atom probe tomography. *Ultramicroscopy* **124**, 96–101. https://doi.org/10.1016/j.ultramic.2012.08.014

Eder K, Felfer PJ, Gault B, Ceguerra AV, La Fontaine A, Masters AF, Maschmeyer T & Cairney JM (2017). A new approach to understand the adsorption of thiophene on different surfaces: An atom probe investigation of self-assembled monolayers. *Langmuir* **33**, 9573–9581. https://doi.org/10.1021/acs.langmuir.7b01820

Estivill R, Audoit G, Barnes J-P, Grenier A & Blavette D (2016). Preparation and analysis of atom probe tips by xenon focused ion beam milling. *Microsc Microanal* **22**, 576–582. https://doi.org/10.1017/S1431927616000581

Evertsson J, Bertram F, Zhang F, Rullik L, Merte LR, Shipilin M, Soldemo M, Ahmadi S, Vinogradov N, Carlà F, Weissenrieder J, Göthelid M, Pan J, Mikkelsen A, Nilsson J-O & Lundgren E (2015). The thickness of native oxides on aluminum alloys and single crystals. *Appl Surf Sci* **349**, 826–832. https://doi.org/10.1016/j.apsusc.2015.05.043

Exertier F, Wang J, Fu J & Marceau RKW (2021). Understanding the effects of graphene coating on the electrostatic field at the tip of an atom probe tomography specimen. *Microsc Microanal* **28**, 1–12. https://doi.org/10.1017/S1431927621012356

Felfer P, Benndorf P, Masters A, Maschmeyer T & Cairney JM (2014). Revealing the distribution of the atoms within individual bimetallic catalyst nanoparticles. *Angew Chem Int Ed Engl* **53**, 11190–11193. https://doi.org/10.1002/anie.201405043

Felfer P, Li T, Eder K, Galinski H, Magyar AP, Bell DC, Smith GDW, Kruse N, Ringer SP & Cairney JM (2015). New approaches to nanoparticle sample fabrication for atom probe tomography. *Ultramicroscopy* **159**, 413–419. https://doi.org/10.1016/j.ultramic.2015.04.014

Forbes RG (1995). Field evaporation theory: A review of basic ideas. *Appl Surf Sci* **87–88**, 1–11. https://doi.org/10.1016/0169-4332(94)00526-5

Fortes MA (1971). General properties of field-ion image projection. *Surf Sci* **28**, 117–131. https://doi.org/10.1016/0039-6028(71)90089-6

Gault B, Chiaramonti A, Cojocaru-Mirédin O, Stender P, Dubosq R, Freysoldt C, Makineni SK, Li T, Moody M & Cairney JM (2021). Atom probe tomography. *Nat Rev Methods Primers* **1**, 1–51. https://doi.org/10.1038/s43586-021-00047-w

Gault B, Cui XY, Moody MP, de Geuser F, Sigli C, Ringer SP & Deschamps A (2012a). Atom probe microscopy investigation of Mg site occupancy within δ′ precipitates in an Al–Mg–Li alloy. *Scr Mater* **66**, 903–906. https://doi.org/10.1016/j.scriptamat.2012.02.021

Gault B, de Geuser F, Stephenson LTLT, Moody MPMP, Muddle BCBC & Ringer SPSP (2008). Estimation of the reconstruction parameters for atom probe tomography. *Microsc Microanal* **14**, 296–305. https://doi.org/10.1017/S1431927608080690

Gault B, Loi ST, Araullo-Peters VJ, Stephenson LT, Moody MP, Shrestha SL, Marceau RKW, Yao L, Cairney JM & Ringer SP (2011). Dynamic reconstruction for atom probe tomography. *Ultramicroscopy* **111**, 1619–1624. https://doi.org/10.1016/j.ultramic.2011.08.005

Gault B, Moody MP, Cairney JM & Ringer SP (2012*b*). *Atom Probe Microscopy*. New York, NY: Springer New York. http://www.springer.com/materials/characterization+%2526+evaluation/book/978-1-4614-3435-1.

Gault B, Moody MP, de Geuser F, Tsafnat G, Fontaine AL, Stephenson LT, Haley D & Ringer SP (2009). Advances in the calibration of atom probe tomographic reconstruction. *J Appl Phys* **105**, 034913. https://doi.org/10.1063/1.3068197

Geiser BP, Larson DJ, Oltman E, Gerstl SS, Reinhard DA, Kelly TF & Prosa TJ (2009). Wide-field-of-view atom probe reconstruction. *Microsc Microanal* **15**(suppl), 292–293. https://doi.org/10.1017/S1431927609098249

Gordon LM & Joester D (2011). Nanoscale chemical tomography of buried organic-inorganic interfaces in the chiton tooth. *Nature* **469**, 194–197. https://doi.org/10.1038/nature09686

Gordon LM, Tran L & Joester D (2012). Atom probe tomography of apatites and bone-type mineralized tissues. *ACS Nano* **6**, 10667–-10675. https://doi.org/10.1021/nn3049957

Grandfield K, Micheletti C, Deering J, Arcuri G, Tang T & Langelier B (2022). Atom probe tomography for biomaterials and biomineralization. *Acta Biomater* **148**, 44–60. https://doi.org/10.1016/j.actbio.2022.06.010

Greiwe G-H, Balogh Z & Schmitz G (2014). Atom probe tomography of lithium-doped network glasses. *Ultramicroscopy* **141**, 51–55. https://doi.org/10.1016/j.ultramic.2014.03.007

Harrison P, Zhou X, Das SM, Lhuissier P, Liebscher CH, Herbig M, Ludwig W & Rauch EF (2022). Reconstructing dual-phase nanometer scale grains within a pearlitic steel tip in 3D through 4D-scanning precession electron diffraction tomography and automated crystal orientation mapping. *Ultramicroscopy* **238**, 113536. https://doi.org/10.1016/j.ultramic.2022.113536

Herbig M & Kumar A (2021). Removal of hydrocarbon contamination and oxide films from atom probe specimens. *Microsc Res Tech* **84**, 291–297. https://doi.org/10.1002/jemt.23587

Houard J, Vella A, Vurpillot F & Deconihout B (2010). Optical near-field absorption at a metal tip far from plasmonic resonance. *Phys Rev B* **81**, 125411. https://doi.org/10.1103/PhysRevB.81.125411

Houard J, Vella A, Vurpillot F & Deconihout B (2011). Three-dimensional thermal response of a metal subwavelength tip under femtosecond laser illumination. *Phys Rev B* **84**, 33405. https://doi.org/10.1103/PhysRevB.84.033405

Inghram MG & Gomer R (1955). Massenspektrometrische Untersuchungen der Feldemission positiver Ionen. *Z Naturforsch A* **10**, 863–872. https://doi.org/10.1515/zna-1955-1113

Jeske T, Schmitz G & Kirchheim R (1999). Atom probe field ion microscopy investigation of the early interreaction stages in Al/Ni couples. *Mater Sci Eng A* **270**, 64–68. https://doi.org/10.1016/S0921-5093(99)00230-0

Josten JP & Felfer PJ (2022). Atom probe analysis of nanoparticles through pick and coat sample preparation. *Microsc Microanal* **28**, 1188–1197. https://doi.org/10.1017/S1431927621000465

Kellogg GL (1982). Field ion microscopy and pulsed laser atom-probe mass spectroscopy of insulating glasses. *J Appl Phys* **53**, 6383. https://doi.org/10.1063/1.331509

Kellogg GL & Tsong TT (1980). Pulsed-laser atom-probe field-ion microscopy. *J Appl Phys* **51**, 1184. https://doi.org/10.1063/1.327686

Kelly TF, Nishikawa O, Panitz JA & Prosa TJ (2009). Prospects for nanobiology with atom-probe tomography. *MRS Bull* **34**, 744–750. https://doi.org/10.1557/mrs2009.249

Khalaf MK, Al-Kader DSA & Salh JM (2021). Effect of thickness and type of substrate on optical properties of chromium oxide thin film prepared by sputtering magnetron. *IOP Conf Ser Mater Sci Eng* **1105**, 012065. https://doi.org/10.1088/1757-899X/1105/1/012065

Khanna A, Bhat DG & Payzant EA (2006). Growth and characterization of chromium oxide thin films prepared by reactive ac magnetron sputtering. *J Vac Sci Technol A Vac Surf Films* **24**, 1870–1877. https://doi.org/10.1116/1.2244536

Kim S, Antonov S, Zhou X, Stephenson L, Jung C, El-Zoka A, Schreiber DK, Conroy S, Gault B & Mater J (2022). Atom probe analysis of electrode materials for Li-ion batteries: Challenges and ways forward. *J Mater Chem A* **6**, 4883–5230. https://doi.org/10.1039/D1TA10050E

Kim S-HH, Kang PW, Park OO, Seol J-BB, Ahn J-PP, Lee JY & Choi P-PP (2018). A new method for mapping the three-dimensional atomic distribution within nanoparticles by atom probe tomography (APT). *Ultramicroscopy* **190**, 30–38. https://doi.org/10.1016/j.ultramic.2018.04.005

Kim S-HSH, Lim J, Sahu R, Kasian O, Stephenson LTLT, Scheu C & Gault B (2020). Direct imaging of dopant and impurity distributions in 2D MoS2. *Adv Mater* **32**, e1907235. https://doi.org/10.1002/adma.201907235

Kölling S & Vandervorst W (2009). Failure mechanisms of silicon-based atom-probe tips. *Ultramicroscopy* **109**, 486–491. https://doi.org/10.1016/j.ultramic.2008.11.013

La Fontaine A, Gault B, Breen A, Stephenson L, Ceguerra AVV, Yang L, Dinh Nguyen T, Zhang J, Young DJJ & Cairney JMM (2015). Interpreting atom probe data from chromium oxide scales. *Ultramicroscopy* **159**, 354–359. https://doi.org/10.1016/j.ultramic.2015.02.005

Larson DJ, Cerezo A, Juraszek J, Hono K & Schmitz G (2009). Atom-probe tomographic studies of thin films and multilayers. *MRS Bull* **34**, 732–737. https://doi.org/10.1557/mrs2009.247

Larson DJ, Gault B, Geiser BP, De Geuser F & Vurpillot F (2013*b*). Atom probe tomography spatial reconstruction: Status and directions. *Curr Opin Solid State Mater Sci* **17**, 236–247. https://doi.org/10.1016/j.cossms.2013.09.002

Larson DJ, Giddings AD, Wu Y, Verheijen MA, Prosa TJ, Roozeboom F, Rice KP, Kessels WMM, Geiser BP & Kelly TF (2015). Encapsulation method for atom probe tomography analysis of nanoparticles. *Ultramicroscopy* **159**, 420–426. https://doi.org/10.1016/j.ultramic.2015.02.014

Larson D, Prosa T, Bunton J, Olson D, Lawrence D, Oltman E, Strennin S & Kelly T (2013a). Improved mass resolving power and yield in atom probe tomography. *Microsc Microanal* **19**, 994–995. https://doi.org/10.1017/S143192761300696X

Larson DJ, Prosa TJ, Ulfig RM, Geiser BP & Kelly TF (2013c). *Local Electrode Atom Probe Tomography*, pp. 318. New York: Springer Science. https://doi.org/10.1007/978-1-4614-8721-0

Larson DJ, Russell KF & Miller MK (1999). Effect of specimen aspect ratio on the reconstruction of atom probe tomography data. *Microsc Microanal* **5**, 930–931. https://doi.org/10.1017/S1431927600017979

Lefebvre-Ulrikson W, Vurpillot F & Sauvage X (2016). *Atom Probe Tomography: Put Theory into Practice*. Cambridge, MA: Academic Press.

Li Y, Zanders D, Meischein M, Devi A & Ludwig A (2021). Investigation of an atomic-layer-deposited Al_2O_3 diffusion barrier between Pt and Si for the use in atomic scale atom probe tomography studies on a combinatorial processing platform. *Surf Interface Anal* **53**, 727–733. https://doi.org/10.1002/sia.6955

Lim J, Kim S-HSH, Aymerich Armengol R, Kasian O, Choi P-PPP, Stephenson LTLT, Gault B & Scheu C (2020). Atomic-scale mapping of impurities in partially reduced hollow TiO_2 nanowires. *Angew Chem Int Ed Engl* **59**, 5651–5655. https://doi.org/10.1002/anie.201915709

Loi ST, Gault B, Ringer SP, Larson DJ & Geiser BP (2013). Electrostatic simulations of a local electrode atom probe: The dependence of tomographic reconstruction parameters on specimen and microscope geometry. *Ultramicroscopy* **132**, 107–113. https://doi.org/10.1016/j.ultramic.2012.12.012

Mancini L, Amirifar N, Shinde D, Blum I, Gilbert M, Vella A, Vurpillot F, Lefebvre W, Lardé R, Talbot E, Pareige P, Portier X, Ziani A, Davesnne C, Durand C, Eymery J, Butté R, Carlin J-F, Grandjean N & Rigutti L (2014). Composition of wide bandgap semiconductor materials and nanostructures measured by atom probe tomography and its dependence on the surface electric field. *J Phys Chem C* **118**, 24136–24151. https://doi.org/10.1021/jp5071264

Melmed AJ (1991). The art and science and other aspects of making sharp tips. *J Vac Sci Technol B* **9**, 601–608. https://doi.org/10.1116/1.585467

Miller RA & Holland HJ (1997). Crystallographic orientation of sputtered Cr films on glass and glass–ceramic substrates. *Thin Solid Films* **298**, 182–186. https://doi.org/10.1016/S0040-6090(96)09206-1

Miller MK & Smith GDW (1989). *Atom Probe Microanalysis: Principles and Applications to Materials Problems*. Pittsburg, PA: Materials Research Society.

Mosiman DS, Chen Y-S, Yang L, Hawkett B, Ringer SP, Mariñas BJ & Cairney JM (2021). Atom probe tomography of encapsulated hydroxyapatite nanoparticles. *Small Methods* **5**, 2000692. https://doi.org/10.1002/smtd.202000692

Moy CKS, Ranzi G, Petersen TC & Ringer SP (2011). Macroscopic electrical field distribution and field-induced surface stresses of needle-shaped field emitters. *Ultramicroscopy* **111**, 397–404. https://doi.org/10.1016/j.ultramic.2011.01.024

Müller EW, Panitz JA & McLane SB (1968). The atom-probe field ion microscope. *Rev Sci Instrum* **39**, 83–86. https://doi.org/10.1063/1.1683116

Nishikawa O & Kato H (1986). Atom-probe study of a conducting polymer: The oxidation of polypyrrole. *J Chem Phys* **85**, 6758–6764. https://doi.org/10.1063/1.451407

Perea DE, Gerstl SSA, Chin J, Hirschi B & Evans JE (2017). An environmental transfer hub for multimodal atom probe tomography. *Adv Struct Chem Imaging* **3**, 12. https://doi.org/10.1186/s40679-017-0045-2

Perea DE, Wijaya E, Lensch-Falk JL, Hemesath ER & Lauhon LJ (2008). Tomographic analysis of dilute impurities in semiconductor nanostructures. *J Solid State Chem* **181**, 1642–1649. https://doi.org/10.1016/j.jssc.2008.06.007

Prosa T, Alvis R, Tsakalakos L & Smentkowski V (2008). Analysis of silicon nanowires by laser atom probe tomography prepared by a protected lift-out processing technique. *Microsc Microanal* **14**, 456–457. https://doi.org/10.1017/S1431927608083761

Prosa T, Kostrna Keeney S & Kelly TF (2010). Local electrode atom probe analysis of poly(3-alkylthiophene)s. *J Microsc* **237**, 155–167. https://doi.org/10.1111/j.1365-2818.2009.03320.x

Prosa TJ & Larson DJ (2017). Modern focused-ion-beam-based site-specific specimen preparation for atom probe tomography. *Microsc Microanal* **23**, 194–209. https://doi.org/10.1017/S1431927616012642

Reddy SM, Saxey DW, Rickard WDA, Fougerouse D, Montalvo SD, Verberne R & van Riessen A (2020). Atom probe tomography: Development and application to the geosciences. *Geostand Geoanal Res* **44**, 5–50. https://doi.org/10.1111/ggr.12313

Schmidt WA, Melmed AJ, Lovisa MF, Naschitzi M & Block JH (1988). Field-ion energy spectroscopy of gold overlayers on silicon. *Surf Sci* **194**, 127–135. https://doi.org/10.1016/0039-6028(94)91249-1

Schreiber DK, Perea DE, Ryan JV, Evans JE & Vienna JD (2018). A method for site-specific and cryogenic specimen fabrication of liquid/solid interfaces for atom probe tomography. *Ultramicroscopy* **194**, 89–99. https://doi.org/10.1016/j.ultramic.2018.07.010

Seol JB, Kwak CM, Kim YT & Park CG (2016). Understanding of the field evaporation of surface modified oxide materials through transmission electron microscopy and atom probe tomography. *Appl Surf Sci* **368**, 368–377. https://doi.org/10.1016/j.apsusc.2016.01.196

Sha G, Cerezo A & Smith GDW (2008). Field evaporation behavior during irradiation with picosecond laser pulses. *Appl Phys Lett* **92**, 043503. https://doi.org/10.1063/1.2837626

Singh MP, Woods EV, Kim S-H, Jung C, Aota LS & Gault B (2023). Facilitating the systematic nanoscale study of battery materials by atom probe tomography through in-situ metal coating. *Batter Supercaps* e202300403. https://doi.org/10.1002/batt.202300403

Southon MJ, Boyes ED, Turner PJ & Waugh AR (1975). Some applications of field-ionization and field-evaporation techniques in the study of surfaces. *Surf Sci* **53**, 554–580. https://doi.org/10.1016/0039-6028(75)90154-5

Stintz A & Panitz JA (1991). Imaging atom-probe analysis of an aqueous interface. *J Vac Sci Technol A Vac Surf Films* **9**, 1365–1367. https://doi.org/10.1116/1.577628

Tamion A, Cadel E, Bordel C & Blavette D (2006). Three-dimensional atom probe investigation of Fe/Dy multilayers. *Scr Mater* **54**, 671–675. https://doi.org/10.1016/j.scriptamat.2005.10.036

Taylor SD, Liu J, Arey BW, Schreiber DK, Perea DE & Rosso KM (2018). Resolving iron(II) sorption and oxidative growth on hematite (001) using atom probe tomography. *J Phys Chem C* **122**, 3903–3914. https://doi.org/10.1021/acs.jpcc.7b11989

Tegg L, Breen AJ, Huang S, Sato T, Ringer SP & Cairney JM (2023). Characterising the performance of an ultrawide field-of-view 3D atom probe. *Ultramicroscopy* **253**, 113826. https://doi.org/10.1016/j.ultramic.2023.113826

Thompson K, Lawrence D, Larson DJ, Olson JD, Kelly TF & Gorman B (2007). In situ site-specific specimen preparation for atom probe tomography. *Ultramicroscopy* **107**, 131–139. https://doi.org/10.1016/j.ultramic.2006.06.008

Vovk V, Schmitz G, Hutten A & Heitmann S (2007). Mismatch-induced recrystallization of giant magneto-resistance (GMR) multilayer systems. *Acta Mater* **55**, 3033–3047. https://doi.org/10.1016/j.actamat.2006.12.036

Vurpillot F, Gault B, Vella A, Bouet M & Deconihout B (2006). Estimation of the cooling times for a metallic tip under laser illumination. *Appl Phys Lett* **88**, 94105. https://doi.org/10.1063/1.2181654

Vurpillot F, Houard J, Vella A & Deconihout B (2009). Thermal response of a field emitter subjected to ultra-fast laser illumination. *J Phys D Appl Phys* **42**, 125502. https://doi.org/10.1088/0022-3727/42/12/125502

Wilkes TJ, Titchmar JM, Smith GDW, Smith DA, Morris RF, Johnston S, Godfrey TJ & Birdseye P (1972). Fracture of field-ion microscope specimens. *J Phys D Appl Phys* **5**, 2226–2230. https://doi.org/10.1088/0022-3727/5/12/312

Wittmaack K & Oppolzer H (2011). Quantitative characterization of xenon bubbles in silicon: Correlation of bubble size with the damage generated during implantation. *Nucl Instrum Methods Phys Res B Beam Interact Mater Atoms* **269**, 380–385. https://doi.org/10.1016/j.nimb.2010.11.025

Woods EV, Singh MP, Kim S-H, Schwarz TM, Douglas JO, El-Zoka AA, Giulani F & Gault B (2023). A versatile and reproducible cryo-sample preparation methodology for atom probe studies. *Microsc Microanal* **29**, 1992–2003. https://doi.org/10.1093/micmic/ozad120

Zhang S, Gervinskas G, Liu Y, Marceau RKW & Fu J (2021). Nanoscale coating on tip geometry by cryogenic focused ion beam deposition. *Appl Surf Sci* **564**, 150355. https://doi.org/10.1016/j.apsusc.2021.150355

TESCAN
PERFORMANCE IN NANOSPACE

TESCAN FIB-SEM

Drive your materials development
and get comprehensive answers.

Fast and effortless!

info.tescan.com/matsci-fib-sem

Scan for more information